JOURNAL OF SPACECRAFT AND ROCKETS
Vol. 41, No. 3, May–June 2004

Turbulence Structure of a Compressible Base Flow with a Central Bleed Jet

C. J. Bourdon* and J. C. Dutton†
University of Illinois at Urbana—Champaign, Urbana, Illinois 61801

The turbulent structures present in the outer shear layer of an axisymmetric, compressible base flow with a central bleed jet are examined with a planar Mie-scattering imaging technique. The effects of bleed rate on the mean size, shape, and orientation of large-scale structures and the steadiness of the shear layer itself are quantified through the use of spatial correlation, shape factor, and steadiness analyses. This study demonstrates that the bleed fluid significantly influences the evolution of the turbulent structures in the outer shear layer. The presence of the bleed jet enforces symmetry on the flowfield and reduces turbulent-structure interaction across the centerline, significantly decreasing end-view centroidal fluctuations throughout the flowfield. Increased mass injection into the separated region and increased base pressure lead to spanwise-dominated mean turbulent structure statistics near the base. As the bleed flow rate is increased, the recompression shock system weakens, and the dramatic increase in structure size seen in the no-bleed case between the recompression and reattachment imaging positions becomes less prominent. The differences in turbulent structure size, shape, and orientation as a result of mass injection into the base region appear to vanish as the structures pass downstream into the developing wake region. In the absence of strong pressure gradients and streamline convergence effects, the surviving turbulent structures seem to have a preferred size and orientation that is dependent only on their proximity to the symmetry line of the wake.

Nomenclature

A	=	area
$A, B1, B2, C, D, E$	=	imaging positions
a	=	major axis
b	=	minor axis
h	=	horizontal
M	=	Mach number
M_c	=	convective Mach number
Re	=	Reynolds number
r	=	radius
x, y, z	=	cardinal axes
δ	=	shear-layer thickness

Superscripts and Subscripts

base	=	property of the base
cen	=	relative to the end-view centroid
end	=	end view
local	=	local property
r	=	reattachment
side	=	side view
$\prime$	=	fluctuation

Introduction

RESEARCHERS have shown that under highly compressible conditions cold-bleed gas injected into the base region can reduce the overall drag of a projectile by up to 10% and can lead to even higher drag reductions if hot gas or reacting gases are used. For the cold-bleed condition much of the benefit gained from base bleed is caused by alteration of the mixing character of the base region caused by the additional mass present in this region. Because mixing is poorly understood in highly compressible, supersonic separated flows, it is of critical importance to examine experimentally flowfields of this type if advances in flow control or further drag reduction are to be made.

The general features of a base region flowfield with mass injection through a central bleed orifice are depicted in Fig. 1. The outer flow remains very similar to that of the no-bleed case. As the freestream flow passes the base corner termination point and separates, an expansion fan forms to accommodate the pressure decrease in the base region and directs the mean flow toward the centerline. A separated shear layer forms between the supersonic outer flow and the low-speed flow immediately behind the base. As the shear layer approaches the axis of symmetry, a recompression shock system forms, redirecting the flow along the streamwise axis. The flow adjacent to the base, however, is significantly altered by mass injection. Low-speed fluid injected into the base region displaces the forward stagnation point downstream of the base plane. The reattachment shock strength is diminished because injected fluid supplies at least a portion of the mass necessary for the shear-layer entrainment process, altering the base pressure and base drag.

A semi-empirical component-type model has been developed to describe the effects of mass injection on the structure of the near wake.[1,2] Even though these models do not account for the instantaneous flow structure, they reasonably capture the mean velocity field and base pressure for a wide range of bleed flow rates. The base-bleed flowfield is classified into three regimes based on the amount of mass injected. A nondimensional injection parameter I has been defined to quantify the magnitude of the bleed flow rate in order to characterize and compare the effectiveness of various bleed flow geometries and mechanisms. This injection parameter is defined as the bleed mass flow rate normalized by the product of the base area and freestream mass flux.

For low values of the injection parameter, the injected fluid provides only a portion of the mass entrained into the shear layer. The base pressure increases approximately linearly with the injection parameter because the amount of recirculating fluid is decreased and the recompression shock system is weakened. This region is defined as regime I. When the bleed flow rate is sufficient to provide all of the fluid entrained by the shear layer, regime II begins. For the current facility Mathur[3] has determined that the transition point between regimes I and II occurs for an injection parameter value

Received 20 July 2002; revision received 30 March 2003; accepted for publication 2 July 2003. Copyright © 2003 by the American Institute of Aeronautics and Astronautics, Inc. All rights reserved. Copies of this paper may be made for personal or internal use, on condition that the copier pay the $10.00 per-copy fee to the Copyright Clearance Center, Inc., 222 Rosewood Drive, Danvers, MA 01923; include the code 0022-4650/04 $10.00 in correspondence with the CCC.

*Graduate Research Assistant, Department of Mechanical and Industrial Engineering; currently Senior Member Technical Staff, Sandia National Laboratories, P.O. Box 5800, MS 0834, Albuquerque, NM 87185. Member AIAA.

†W. Grafton and Lillian B. Wilkins Professor, Department of Mechanical and Industrial Engineering. Associate Fellow AIAA.

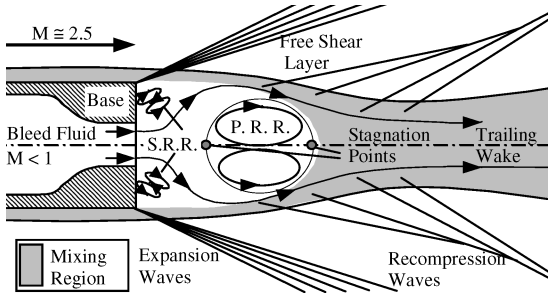

Fig. 1 Schematic of mean base-bleed flowfield. The primary recirculation region is labeled P. R. R., and the secondary recirculation region is labeled S. R. R.

of $I = 0.0148$. For this injection rate the maximum base pressure is realized, and the recompression shock system is considerably weakened from the no-bleed case. As the injection parameter is increased beyond this optimal value, both the recompression shock system and primary recirculation region decrease significantly in strength with increasing injection rates. For very high injection rates the bleed flow acts as a highly underexpanded jet, and power-on propulsion is obtained. These conditions are described as regime III. This regime is also characterized by increasing base pressure with increasing bleed flow rate.

Since the advent of laser-based diagnostic techniques, it has been possible to obtain detailed pointwise and planar information about the instantaneous structure of the base-bleed flowfield. Mathur and Dutton[4,5] have measured the mean velocity and turbulence fields in the near wake of a cold-bleed case with a fixed central-bleed orifice and a freestream Mach number of 2.46. Bourdon and Dutton[6] directly visualized the central-bleed jet using an acetone planar laser-induced fluorescence (PLIF) technique. These studies have shown that the Korst[2] model adequately describes the average structure of the base-bleed flowfield. Mathur and Dutton[4] further indicate that there is an overall reduction in turbulence levels throughout the base-bleed flowfield at all bleed conditions that were examined relative to the no-bleed case. Their study demonstrated that the overall turbulent kinetic energy in the near-wake region is minimum at the maximum base-pressure point. Additionally, they showed that the formation of a strong secondary recirculation region near the base annulus and a strong bleed-jet shear layer are responsible for the drop in base pressure that offsets the benefit of base bleed at postoptimal bleed rates. Bourdon and Dutton's study showed that the instantaneous structure of the bleed jet significantly affects the entrainment characteristics of the outer shear layer. Ejection of bleed fluid into the outer shear layer, symmetric breakup of the bleed jet, and formation of an inner shear layer along the outer edge of the bleed jet all play key roles in the evolution of the near-wake flow structure.

The base-bleed flowfield has also been examined computationally.[7–10] Because of the high Reynolds numbers associated with realistic applications of supersonic projectiles, these computational efforts have been limited to Reynolds-averaged Navier–Stokes (RANS)-type calculations. These computations have demonstrated the ability to capture many of the mean features of the base flowfield, but have not adequately described the turbulence field, particularly near stagnation points. This discrepancy occurs because the turbulence models typically employed in these computations do not accurately describe the turbulence present in this complex flow.[11] More data are therefore necessary to gain a thorough understanding of the turbulence mechanisms in these high-speed separated flows with mass injection.

Bourdon and Dutton[12–15] have employed a planar Rayleigh/Mie-scattering technique to visualize the turbulent structures present in the separated shear layer behind a range of afterbodies. This technique provides valuable information about the instantaneous size, shape, and organization of turbulent structures in the near-wake region and enhances the interpretation of previously obtained mean velocity and turbulence data in comparable flowfields.[16,17] By applying this technique to the current base-bleed geometry, comparisons can likewise be made to both existing velocity data[4,5] and laser-induced fluorescence visualizations of the central bleed jet[6] to further our understanding of the complex interactions between the jet, recirculating, and freestream fluids and the mechanisms that affect the evolution of the near-wake flowfield. This study represents the first effort to quantify the instantaneous structure of the shear layer of a supersonic base-bleed flowfield.

Flow Facility and Equipment

These experiments were conducted in a facility specifically designed for studying base flow phenomena about and behind cylindrical afterbodies. A complete description of the flow facility is given by Sauter.[18] For the sake of brevity, the current description is limited to a brief review and schematic of the wind tunnel and flow-visualization equipment used in these experiments (Fig. 2). Three large windows have been fitted into the test section to allow for the passage of a laser sheet and off-axis viewing of the near wake. These windows allow full optical access to the near-wake region.

The facility is a blowdown-type facility, with compressed air supplied from a series of storage tanks with a volume of 140 m^3 pumped up to 930 kPa at 34 m^3/s. The air is dried and cleansed of all particulates before each blowdown. The plenum pressure is maintained constant to within 0.25% rms pressure deviation by a control valve driven by a proportional–integral–derivative controller-type three-stage controller. The flow conditioning module and supersonic nozzle provide a uniform supersonic freestream flow of relatively low turbulence intensity ($< 1\%$) at a nominal freestream Mach number of 2.46 and a unit Reynolds number of $Re = 52 \times 10^6$ m^{-1} for nominal operating conditions.[17] The turbulent boundary-layer thickness on the sting/afterbody just before separation is approximately 3.2 mm (Ref. 17). The diameter of the facility converging-diverging nozzle at its exit plane is approximately 20.3 cm.

While conducting these base-bleed experiments, bleed flow was supplied to the base through two modifications to the wind tunnel. A stainless-steel bleed line, designed by Mathur[3] and constructed from 5.1-cm-diam stainless-steel tubing, was attached to the upstream end of the sting. An electronic flow meter, operating on the hot-wire principle, was used to monitor the mass flow rate through the bleed line. The flow meter was calibrated for a range of 0–42.5 g/s and is rated to an accuracy of $+/-0.5\%$ of the reading plus 1% of full scale. A butterball valve was used for coarse bleed flow control, while a needle valve was placed in parallel to the butterball valve for fine bleed flow control.

The second modification necessary for these bleed flow experiments was the insertion of an afterbody base with a 25.4-mm-diam bleed orifice, also designed by Mathur.[3] The 63.5-mm outer diameter afterbody and orifice were designed to produce unchoked flow at the bleed exit for all of the bleed conditions examined in the present study. This afterbody base is also equipped with a series of pressure taps, so that the effect of bleed rate on the base pressure can be measured.

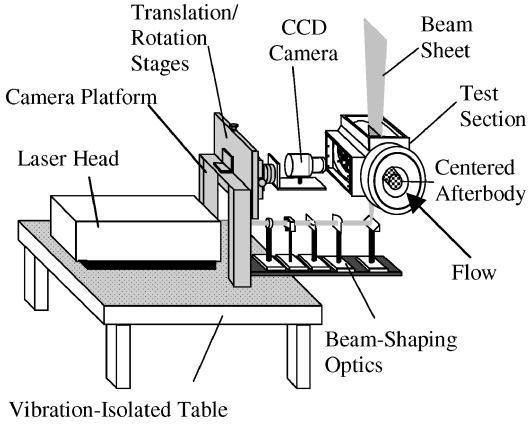

Fig. 2 Mie-scattering image acquisition system.

Passive Scalar Ethanol Mie Scattering

The present study implements the same Mie-scattering technique used by Smith.[19] Ethanol vapor is carried in the supply air that approaches the converging-diverging nozzle, and, as it undergoes a rapid expansion and is accelerated supersonically within the nozzle, the vapor condenses into a fine mist. The mean condensed droplet diameter is approximately 0.05 μm,[19] which is easily small enough to mark and track the large-scale turbulent structures of interest here[20]

The saturation characteristics of ethanol are such that, in the facility used in this study, the ethanol fog will vaporize (or condense) at flow speeds that correspond with approximately sonic conditions.[19] The initial fog formation occurs at a supersaturation ratio of approximately 12 (Ref. 21), indicating that homogeneous condensation will dominate the condensation process, leading to a small, uniform droplet size.[22] Because the shear layer in a supersonic blunt-base flowfield separates a subsonic recirculation region from a supersonic freestream, the ethanol seed marks the interface (i.e., shear layer) between these two regions quite well.

This ethanol fog is illuminated by 532-nm light supplied from a Nd:YAG laser. The output beam is formed into a thin laser sheet, approximately 200 μm thick at the beam waist, by a series of beam-shaping optics and is used to illuminate a thin slice of the condensed ethanol mist (Fig. 2). Because the laser pulse duration is only 6–8 ns, it is short enough to allow for unsmeared images to be collected. The scattered light is collected by a high-resolution 14-bit unintensifed back-illuminated charge-coupled-device (CCD) camera for analysis. Because the images are obtained from a passive scalar on an essentially instantaneous basis, the reader is cautioned about drawing unwarranted conclusions concerning the dynamic, vortical nature of this flow from these images.

Results and Discussion

A detailed imaging study of passive scalar Mie scattering from condensed ethanol droplets seeded into the outer freestream is performed to quantify the evolution of the large-scale structures present in the outer shear layer. Three bleed rates are examined in detail: a low-bleed case (bleed case A), a slightly preoptimal bleed case (bleed case B), and a postoptimal bleed case (bleed case C). These bleed rates were chosen both because they highlight the primary changes in overall separated flowfield structure and because they correspond with the bleed cases examined by Mathur.[3] Imaging locations were chosen to help identify how and why turbulent motions and the mean turbulent structures evolve in the near wake with base bleed. These imaging locations are described in Table 1 and are graphically displayed (in the side-view orientation) in Fig. 3 for all three bleed cases. The imaging position labels were chosen to correspond approximately to previous imaging studies of compressible near wakes.[6,12–15,23]

Because the central bleed jet pushes the forward stagnation point downstream and subsequently leads to the development of a secondary recirculation region in the annulus between the bleed jet and outer flow, the turbulent structures present at the initial imaging positions (A, $B1$, and $B2$) are subject to many effects that are not present in the no-bleed case. The evolution of the turbulent structures and the turbulent motions of the shear layer itself will reflect the added complexity generated by interaction with the bleed-jet fluid. For instance, bleed fluid is ejected outward and into the shear layer at the first imaging position A of bleed case A[6] and at the third imaging position $B2$ of bleed case B.[6] Effects similar to those seen in the recompression and reattachment processes for the no-bleed case (positions C and D of Ref. 12) should be evident in the statistics for bleed cases B (position $B1$) and C (positions $B1$ and $B2$) because of this added complexity.

Ensembles of approximately 500 images have been acquired at each imaging position in both the side and end views for all three bleed cases, in accordance with the standard set by Smith[19] to provide converged statistics. Steadiness, shape factor, and spatial correlation analysis techniques are applied to the image ensembles to quantify the nature of the large-scale turbulent structures and motions evident in the shear layers for all three bleed cases. The results of this analysis are then compared to the no-bleed case to determine how the bleed jet alters the development of the near-wake region. When this analysis is viewed in conjunction with acetone PLIF images of the central bleed jet,[6] a comprehensive picture of the near-wake region and the effect that mass injection plays in altering its evolution is obtained.

Instantaneous Images

Instantaneous side-view images from positions $B1$, $B2$, C, D, and E are presented for bleed cases A, B, and C in Figs. 4–6,

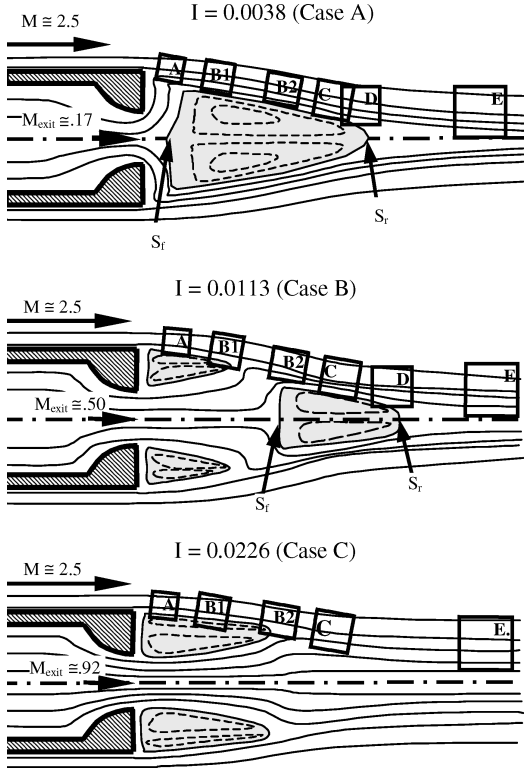

Fig. 3 Flowfield schematic and imaging positions for ethanol planar Mie-scattering study for bleed cases A, B, and C.

Table 1 Coordinates at imaging positions for bleed cases A, B, and C

	Bleed case A		Bleed case B		Bleed case C	
Imaging position	Location	Distance from base, x/R_{base}	Location	Distance from base, x/R_{base}	Location	Distance from base, x/R_{base}
A	F. S. P.[a]	0.3	Shear layer	0.3	Shear layer	0.3
$B1$	Shear layer	1.2	Recompression[b]	1.2	Recompression[b]	1.2
$B2$	Shear layer	1.8	F. S. P.[a]	1.8	R. S. P.[c]	1.8
C	Recompression	2.7	Recompression	2.7	Recompression	2.7
D	Reattachment	3.1	Reattachment	3.3	——	——
E	Near wake	4.25	Near wake	4.25	Near wake	4.25

[a]Forward stagnation point of primary recirculation region.
[b]Recompression caused by secondary recirculation region.
[c]Rear stagnation point of secondary recirculation region.

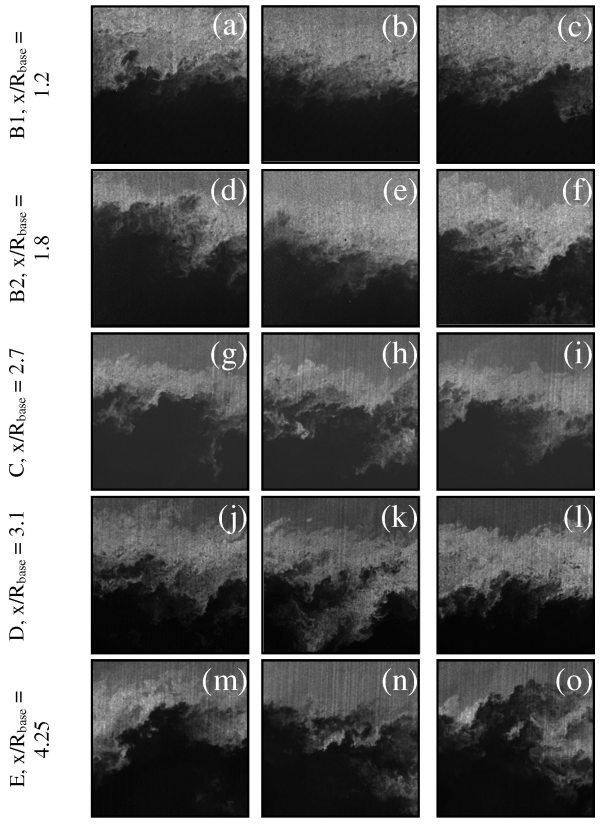

Fig. 4 Instantaneous side-view ethanol passive scalar Mie-scattering images of bleed case A ($I = 0.0038$) at image positions *B*1 (a, b, and c), *B*2 (d, e, and f), *C* (g, h, and i), *D* (j, k, and l), and *E* (m, n, and o). Each frame is approximately $3\delta \times 3\delta$ in dimension.

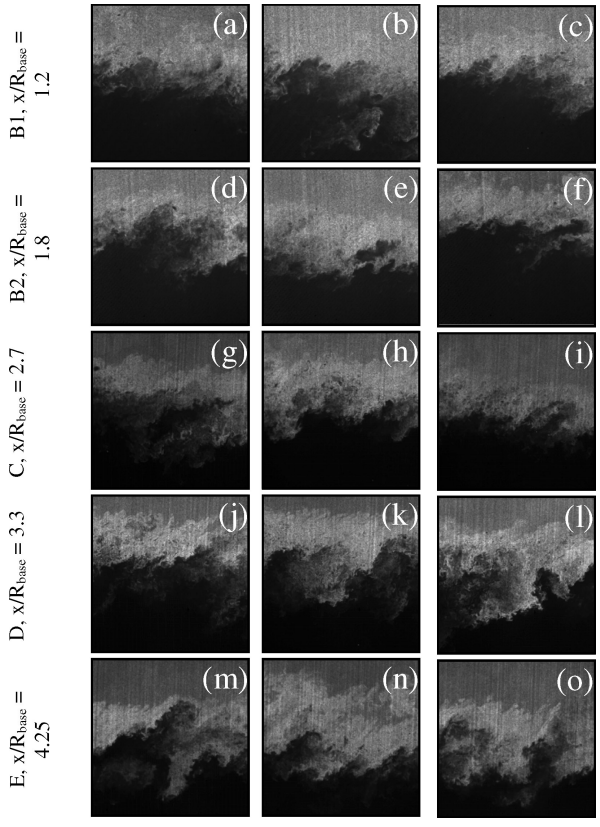

Fig. 5 Instantaneous side-view ethanol passive scalar Mie-scattering images of bleed case B ($I = 0.0113$) at image positions *B*1 (a, b, and c), *B*2 (d, e, and f), *C* (g, h, and i), *D* (j, k, and l), and *E* (m, n, and o). Each frame is approximately $3\delta \times 3\delta$ in dimension.

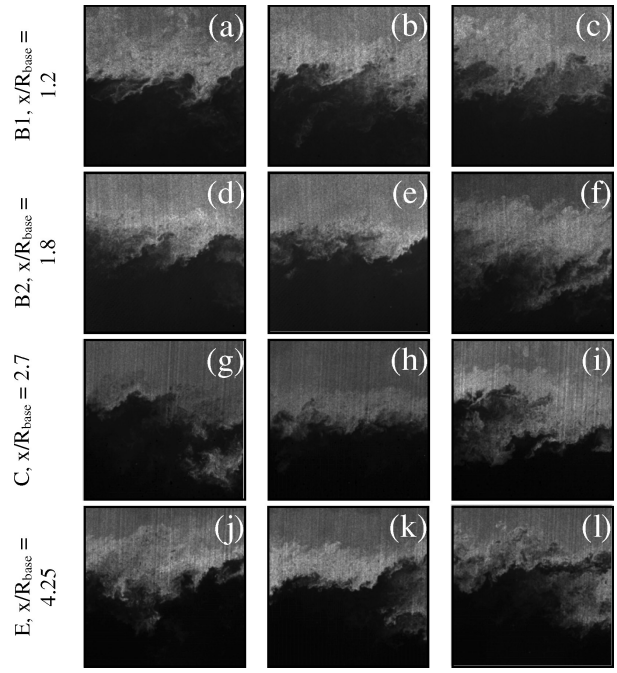

Fig. 6 Instantaneous side-view ethanol passive scalar Mie-scattering images of bleed case C ($I = 0.0226$) at image positions *B*1 (a, b, and c), *B*2 (d, e, and f), *C* (g, h, and i), and *E* (j, k, and l). Each frame is approximately $3\delta \times 3\delta$ in dimension.

respectively. End-view instantaneous images of the same imaging positions for all three bleed conditions are presented in Figs. 7–9. Images from position A were excluded from these figures because the qualitative features evident in the images are virtually identical to those seen in the no-bleed case. The side-view images (Figs. 4–6) have been cropped such that the horizontal and vertical axes, which are tangent and normal to the mean local flow direction, are approximately three local shear-layer thicknesses in size to facilitate a comparison between the different imaging positions. The end-view images (Figs. 7–9) have been scaled so that the outer frame of each image corresponds to 2.1 base radii.

At all three bleed rates, the instantaneous side-view images show the same details as seen in the no-bleed case: stringy, filament-like structures extend from the high-speed (high-signal) freestream and trail into the low-speed (and low-signal) wake-core region. Additionally, fingers of core fluid are ejected outward into the freestream fluid and are accelerated downstream as the two regions mix. Because the shear layer is highly compressible ($M_c > 1$) for imaging positions A–D for all bleed conditions, the turbulent structure organization is highly three-dimensional and irregular in nature and is difficult to characterize through inspection of individual images. Generally, the turbulent structures are elliptic or elongated in shape and inclined with respect to the local flow direction toward the high-speed stream. For all bleed cases individual large-scale structures tend to dominate a larger portion of the shear layer at downstream imaging positions than at imaging positions *A* and *B*1.

Bleed Case A

For bleed case A (Figs. 4 and 7), the amount of mass injected into the base region ($I = 0.0038$) and the jet's axial momentum are minimal, so that the effect that mass injection has on the turbulent structures present in the shear layer is expected to be relatively small for this bleed case. The acetone PLIF images[6] showed that the bleed fluid tends to flow immediately outward toward the outer shear layer as it negotiates a path between the primary recirculation region and the base. Therefore, visible differences in the turbulent structures caused by the mass addition should be evident at imaging positions *A* and *B*1. Because the base pressure is higher for this bleed case than for the no-bleed baseline case, additional differences in the evolution of the turbulent structures could possibly be present in

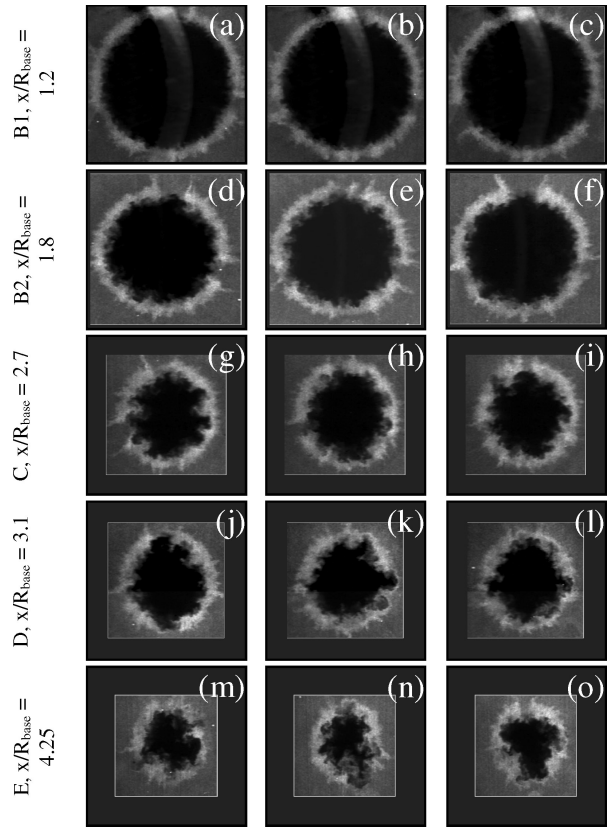

Fig. 7 Instantaneous end-view ethanol passive scalar Mie-scattering images of bleed case A ($I = 0.0038$) at image positions *B*1 (a, b, and c), *B*2 (d, e, and f), *C* (g, h, and i), *D* (j, k, and l), and *E* (m, n, and o). Each frame is approximately 2.1 × 2.1 base radii in dimension.

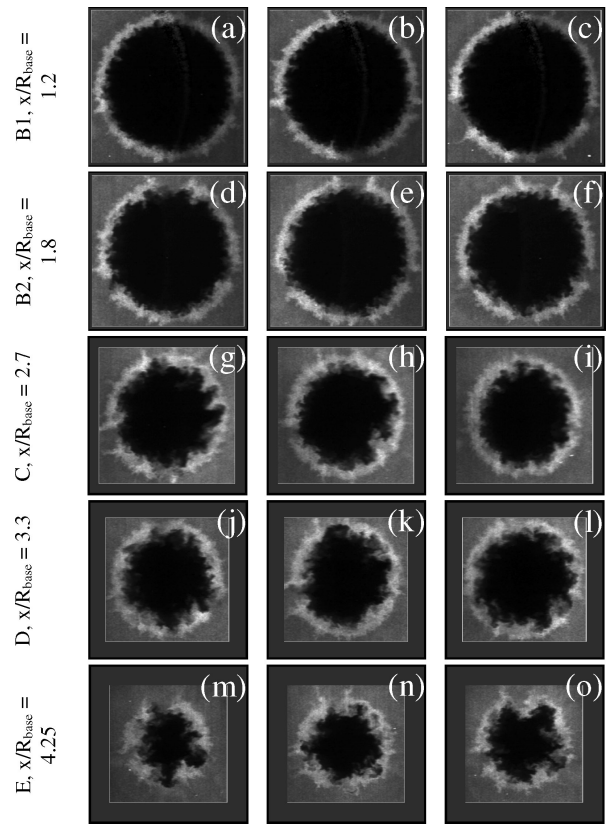

Fig. 8 Instantaneous end-view ethanol passive scalar Mie-scattering images of bleed case B ($I = 0.0113$) at image positions *B*1 (a, b, and c), *B*2 (d, e, and f), *C* (g, h, and i), *D* (j, k, and l), and *E* (m, n, and o). Each frame is approximately 2.1 × 2.1 base radii in dimension.

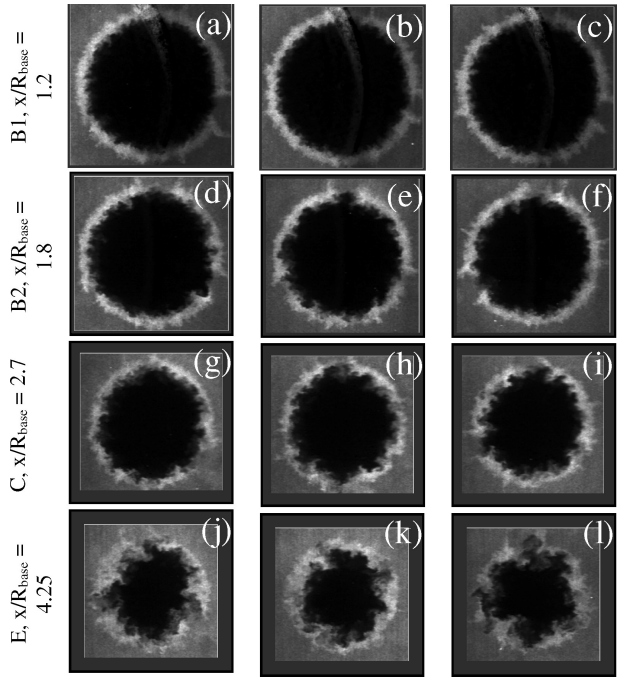

Fig. 9 Instantaneous end-view ethanol passive scalar Mie-scattering images of bleed case C ($I = 0.0226$) at image positions *B*1 (a, b, and c), *B*2 (d, e, and f), *C* (g, h, and i), and *E* (j, k, and l). Each frame is approximately 2.1 × 2.1 base radii in dimension.

the recompression and reattachment process because of the weaker recompression shock system.

Figures 4 and 7 for bleed case A do demonstrate some subtle differences in the turbulent structures evident in the shear layer from the no-bleed case.[12] Because of the added mass available for entrainment into the shear layer from the base region, the turbulent structures appear to be slightly larger in the initial portions of the shear layer and seem to be greater in number. This is not to say that they are more organized because of the mass injection, but rather that there are simply more structures in a given ensemble for bleed case A than without bleed. This could also be the result of the decreased strength of the base corner expansion fan. As shown by Herrin and Dutton,[24] the strength of the base corner expansion can significantly change the turbulence characteristics of the initial portions of the developing shear layer.

The shear-layer position in the end-view instantaneous images (Fig. 7) also appears to be less variable for the ensemble of images because of the mass injection, especially in the developing wake (position *E*). As mass is injected into the base region, the base pressure increases, the recompression shock system weakens, and more mass escapes into the wake core region, leading to a widening of the wake core. As this occurs, the turbulent structures are not forced to interact and amalgamate with their neighbors. This decreased interaction is evident in the larger number of structures that are present in the end views at position *E* (Figs. 7m–7o) for bleed case A than for the no-bleed case. Additionally, as the core region widens, smaller variations in the position of the shear layer displace larger amounts of fluid. The combination of these two phenomena leads to a lower level of apparent fluctuations in the shear-layer position at the latter image locations.

Bleed Case B

For bleed case B ($I = 0.0113$) the bleed jet penetrates approximately one base radius on average into the near wake before it interacts with the outer shear layer.[6] The interaction of bleed fluid with the outer shear layer is evident in the instantaneous passive scalar Mie-scattering images as much larger structures at imaging position *B*1 (Figs. 5a–5c) than are evident in the corresponding images for bleed case A (Figs. 4a–4c) or the no-bleed case.[12] Because the recompression shock structure and primary recirculation region are

significantly weakened because of near-optimal bleed conditions, the structures visible in the images at positions *C* (recompression; Figs. 5g–5i) and *D* (reattachment; Figs. 5j–5l) do not demonstrate the characteristic features attributed to these regions. The turbulent structures do not appear to rotate down toward the local streamwise axis or to grow significantly in size at either imaging positions *C* or *D*.

In the end-view orientation the primary difference in the images of bleed case B (Fig. 8) from bleed case A (Fig. 7) and the no-bleed case[12] is the size of the core fluid (subsonic, low-signal) region. As expected, the core region becomes larger as the base pressure and the amount of bleed fluid escaping into the near wake both increase with bleed rate. Even more turbulent structures are evident in the end-view images from position *E* in the trailing wake (Figs. 8m–8o) for bleed case B: 9–12 structures in each image, as compared to 6–8 for bleed case A and 3–5 for the no-bleed case.

Bleed Case C

Because bleed case C yields a postoptimal drag benefit and the primary recirculation region has disappeared, the turbulent structures in the passive scalar Mie-scattering images (Figs. 6 and 9) appear to be very similar throughout imaging positions *B*1–*E*. The side-view structures (Fig. 6) appear to scale approximately with the local shear-layer thickness and appear to be tilted at roughly the same nominal angle with respect to the local flow direction. This observation is quite sensible because after the bleed-jet fluid passes the secondary recirculation annulus the flow geometry closely resembles a coflowing annular shear layer. The recompression process tends to occur over a longer distance, as is evident in Mathur's shadowgraph and schlieren images,[3] so that the adverse pressure gradient effects will tend to be less significant and occur over a longer distance.

In the end-view orientation (Fig. 9) the instantaneous turbulent structures evolve in a core fluid region that shrinks with downstream distance the least of all three bleed cases because of the amount of bleed fluid injected into the base region. The mean number of structures evident in the instantaneous end-view images at position *E* (Figs. 9j–9l) are thus even larger than for bleed rate B; approximately 10–15 structures are evident in each image. Amalgamation processes must occur in the shear layer for bleed rate *C* mostly because of the growth of individual structures rather than forced interaction caused by lateral streamline convergence.

Average Image Statistics

Shear-layer thickness measurements gathered from the side-view passive scalar Mie-scattering images (supersonic portion of shear layer) are presented in Fig. 10. This figure shows that the base-bleed shear layers all develop in essentially the same manner, but differently than the blunt-base case, especially in the trailing wake. The injection of bleed flow into the base region decreases the shear-layer growth rate near the base slightly because the increased base pressure and decreased base corner expansion strength lead to lower turbulence levels in the initial portion of the shear layer.[4] Between 1.2 and 1.8 base radii downstream of the base corner, the shear layer tends to grow significantly as a result of the injection of bleed fluid

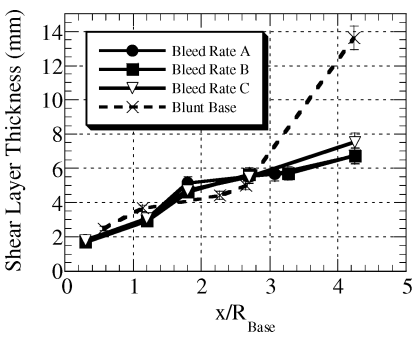

Fig. 10 Mean ethanol passive Mie-scattering shear-layer thickness at all imaging positions of all three base bleed-cases and the blunt-base case. Vertical bars denote uncertainty of the measurements.

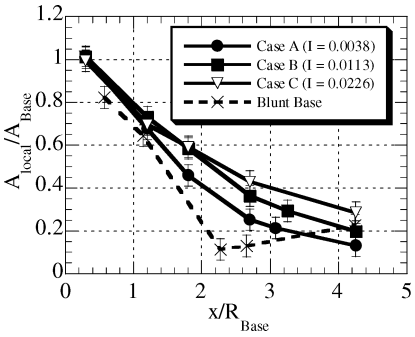

Fig. 11 Mean end-view core area measurements at all imaging positions for all three bleed cases and the blunt-base case, as ascertained from passive scalar ethanol Mie-scattering images. Vertical bars denote uncertainty of the measurements.

into the shear layer. Because the bleed fluid partially inhibits interaction between the outer shear layer and primary recirculation region (cases A and B) or wake core (case C) and significantly reduces the strength of the recompression shock system, the enhancement of shear-layer growth rate evident in the blunt-base case at reattachment and especially in the trailing-wake region is not evident for any of the bleed cases.

The area occupied by core fluid, as seen in the end view, is presented in Fig. 11 for all three bleed cases and the blunt-base case. The most notable difference between the bleed cases and the blunt-base flow is that the minimum of $A_{\text{local}}/A_{\text{base}}$ for the blunt-base case at position *C* ($x/R_{\text{base}} \cong 2.25$) is not present for the three bleed cases. Instead, the core area tends to decrease in size at a continuously slower rate as bleed is increased and appears as if it asymptotes to some finite value in the developing wake. Both the base corner expansion and recompression processes are weakened as a result of the mass addition, and thus the shear layer initially approaches the symmetry line at a shallower angle and is deflected less by the recompression shock system. The expansion of the core area generates the dramatic shear-layer growth in the near wake in the blunt-base case. As the shear layer moves away from the centerline, increased entrainment must occur to maintain a pressure balance between the outer freestream and inner wake regions of the flow. For the base-bleed cases high entrainment rates are not required, as the recompression shock system is not so strong as to impose such a condition.

The initial angle at which the shear layer approaches the centerline depends highly on the base pressure (and, thus, the strength of the base corner expansion), as is evidenced by the approach angles of the initial data points for the three bleed cases (inferred from Fig. 11). Bleed case B, which is associated with the highest base pressure, has the largest local area at position *B*1, 1.2 base radii downstream, whereas bleed case A, which is associated with a lower base pressure, has the smallest local area of the three bleed cases.

By position *C*, $x/R_{\text{base}} = 2.7$, the relative local core fluid area is proportional to the injection parameter. This trend continues throughout the remaining imaging positions. As more mass is supplied to the base region, more low-speed fluid escapes the near wake along the centerline, allowing the shear layer to exist at a position further removed from the centerline.

Interface Convolution Analysis

The convolution or tortuousness of the interface between the outer freestream and inner flow can be used as an estimate of the mixing potential of the interface. This can be quantified by defining a shape factor for specific locations within the flowfield. The shape factor presented here is defined as the ratio of the actual length of the interface to the theoretical minimum interface length. For an enclosed interface, such as the shear layer seen in the current end views, this minimum interface length would be the circumference of a circle encompassing the same area, whereas for an open interface, such as seen in the current side views, the minimum interface length would be that of a straight line connecting the most upstream and downstream boundary points.

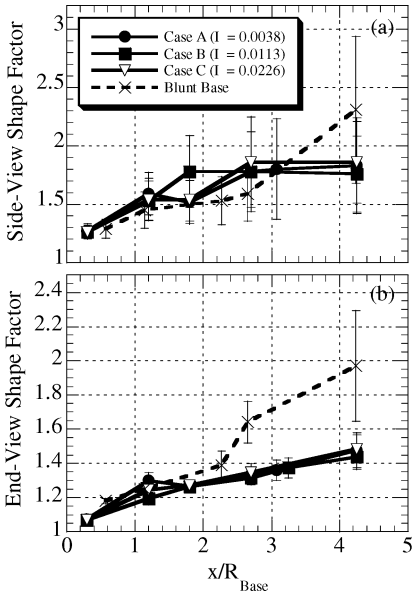

Fig. 12 Shape factor for the blunt-base and all three bleed cases: a) side view and b) end view. Vertical bars denote rms shape factor values (i.e., one standard deviation).

The calculated side-view and end-view shape factors for all three bleed cases and the blunt-base case are presented in Fig. 12. This figure demonstrates that, in the side view, the shape factor values for the base-bleed cases and the blunt-base case in the initial 1.2 base radii after base corner separation are within one standard deviation of each other. Bleed case A has the largest shape factor at position $B1$, most likely because of the injection of bleed fluid in this region.[6] Similarly, where bleed fluid injection nominally occurs for bleed case B, near position $B2$ (1.8 base radii downstream), this bleed case shows much higher shape factor values than the other two bleed cases. At position C and downstream positions the shape factor values for all three bleed cases are very similar and remain relatively constant throughout. This is in direct contrast to the behavior of the no-bleed case, which boasts a much higher shape factor value at imaging position E than at previous positions. As discussed in the preceding section, the increased shape factor for the no-bleed case might be caused by the increased core fluid area at this location (Fig. 11) relative to the two preceding locations. The absence of large shape factor values at location E for the three bleed cases is not surprising because this expansion is not evident in any of the three bleed cases.

In the end view the shape factor (Fig. 12b) is virtually identical for all three bleed cases at all imaging positions, except at position $B1$. The disparity at location $B1$ most likely occurs as a result of two separate effects. The elevated end-view shape factor value for bleed case A is a result of the injection of bleed fluid into the shear layer, whereas the increased value for bleed case C is generated by enhanced mixing in this region caused by the presence of the secondary recirculation region immediately below the shear layer. The enhancement of the end-view shape factor caused by flow reattachment for the blunt-base case is not evident in the data for any of the bleed cases because the shear layer never encroaches on the centerline to the degree that it does for the blunt-base case. Streamline convergence effects, which lead to enhanced flow three-dimensionality and enhanced interaction in the end-view plane, are therefore much less significant as a result of mass injection in the base region.

Shear-Layer Steadiness Analysis

To characterize the unsteady nature of the shear layer, the interface between the freestream and core fluids in the instantaneous images is examined statistically. The bulk shear layer motion is detected by monitoring the location where the scattered light intensity drops to 20% of the freestream value. The shear-layer position (normal to the streamwise direction) in each instantaneous side-view image can then be compared with that of the entire ensemble. In the end view both pulsing (or expansion/contraction) and flapping (or centroidal) motions can be described because the shear layer is nominally a circular, closed curve. The techniques used to determine the shear-layer motion in both the side and end views are described in detail in Ref. 13.

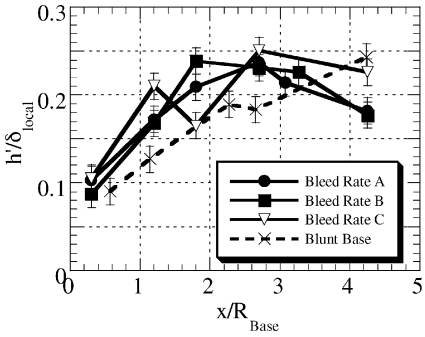

Fig. 13 RMS side-view shear-layer position for the blunt-base and all three base-bleed near-wake flowfields. Vertical bars denote uncertainty of the measurements.

The rms magnitudes of apparent side-view flapping motions are presented in Fig. 13 for bleed cases A, B, and C and the blunt-base case. In all cases the rms magnitude of shear-layer motions remains relatively small, less than 26% of the local shear-layer thickness. A common characteristic of all three bleed cases that distinguishes them from the blunt-base case is that the magnitude of flapping motions decreases with respect to the local shear-layer thickness after the flow transitions into a wake (between positions D and E) instead of increasing, as it does for the blunt-base case. Because of the bleed fluid that is supplied to the base region and escapes into the developing wake region, shear-layer flapping motions actually decrease between positions D and E, rather than increase, as they do for the blunt-base geometry.

The trend of the side-view flapping motions for bleed case A remains similar to that of the blunt-base case through the mean reattachment point, position D, but the flapping motions are approximately 40% larger as a result of the mass injection. This heightened degree of unsteadiness is caused by the unsteady nature of the bleed jet at this flow condition.[6] The magnitude of the flapping motions increases throughout the near-wake region, until the mean reattachment point is reached. At this point the termination of the primary recirculation region dampens the unsteady motions that generate the shear-layer unsteadiness.

The shear-layer unsteadiness evident in the side-view images of bleed case B peak at position $B2$, near the termination of the secondary recirculation region and at the forward stagnation point of the primary recirculation region. It is in this region that the bleed jet breaks apart and bleed fluid is ejected toward the outer shear layer.[6] A maximum in turbulent kinetic energy is also present in the shear layer at this location.[4] The rms fluctuation of shear-layer position for bleed case B remains relatively high at positions C and D, then drops significantly in the developing wake (position E) because of the relaxation of turbulence-generating influences from outside the shear layer.

As the bleed rate is increased from bleed case B to bleed case C, the peak in turbulent kinetic energy that leads to a peak in rms shear-layer position at position $B2$ for bleed case B migrates upstream to position $B1$ (Ref. 4), leading to a local peak in rms shear layer position at this location. A second peak in rms shear-layer position exists at position C, as a result of the breakup of the bleed jet.[6]

The rms position data for the end-view wake core centroid, displayed in Fig. 14 for all three bleed cases and the blunt-base case, do not indicate the dramatic differences between the bleed cases that the side-view flapping data indicate, nor do they display the sloshing motions (at locations C and E) indicated in the blunt-base data. Figure 14 indicates that mass injection results in a significant reduction in the variability of the wake core centroid position for

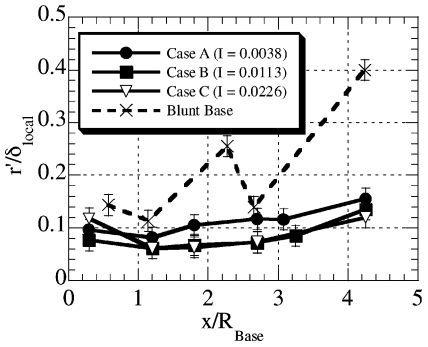

Fig. 14 RMS end-view centroid position fluctuations for the blunt-base and all three base-bleed cases. Vertical bars denote uncertainty of the measurements.

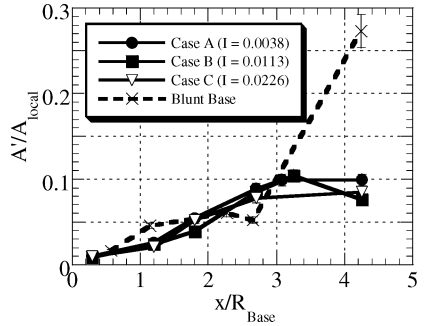

Fig. 15 RMS end-view area fluctuations normalized by the local mean end-view area. Vertical bars denote uncertainty of the measurements.

all imaging positions and bleed rates relative to the no-bleed case. Because the bleed jet is less stationary for bleed case A[6] than for the other-base bleed cases, the rms magnitude of the centroid motion tends to be higher for the low-bleed condition.

The magnitudes of enclosed area fluctuations evident in the end-view images are presented in Fig. 15. The area-based fluctuations also tend to be very similar for the three bleed cases and very different from what is seen in the blunt-base case. Because of the presence of the central bleed jet, area-based fluctuations do not grow as quickly near the base with mass bleed. In the recompression region, position *C*, the area-based fluctuations are greatly enhanced as a result of base bleed. The circumference of the shear layer is much larger for all three bleed cases at positions *B*2, *C*, and *D* than it is for the blunt-base case, and more turbulent structures are present in each image. Therefore, the increase in area fluctuations signifies the intermittent passage of large amounts of fluid through the core region and into the developing wake. This increase in area-based fluctuations without an accompanying increase in centroidal motions (Fig. 14) indicates that the passage of fluid from the base region is generally axisymmetric in nature. This was also indicated in the PLIF images.[6] At position *E* the increased presence of fluid that has escaped the near-wake region without being entrained into the turbulent structures of the outer shear layer greatly diminishes the area-based fluctuations from the levels seen for the blunt-base case.

Spatial Correlation Analysis

A spatial autocorrelation analysis technique, described in detail by Messersmith and Dutton[25] and Smith and Dutton,[26] has been applied to the image ensembles gathered at each imaging position and for each bleed flow rate. This technique is used to ascertain objective information about the mean structure size, shape, and orientation, while limiting the subjectiveness of personal bias. Each correlation field is based on ensembles of approximately 500 images because Smith and Dutton[26] have shown that ensembles of this size produce converged statistics. The 0.5 correlation contour (where the central peak is normalized to a value of 1.0) has been previously established as the basis for determining the mean structure's characteristics.[12,13,23,25,26]

The results of the spatial correlation analysis of all three bleed cases are presented in Figs. 16 (side view) and 17 (end view). The correlation contours are not presented for the three bleed cases because the general characteristics of the contours differ very little from those presented for the other flowfields of this type.[12–15] In the side view the correlation contours are generally elliptic in shape, with the high-speed edge of the structure further downstream than the low-speed side of the structure. In the end view the correlation contours are nominally circular in shape, but tend to be wider on the outer edge than the inner edge because of the annular-shaped shear layer, as seen in the end view.[12]

There is an increase in side-view structure size between imaging positions *A* and *B*1 (Fig. 16, top), as a result of mass injection into the shear layer initiated by the bleed jet.[6] The injection of bleed fluid also leads to slightly more eccentric side-view turbulent structures (Fig. 16, middle) in this region near the base. In the blunt-base case the large-scale structures remain a constant fraction of the local shear-layer thickness in size in this region of the flow. The effect of mass injection is also evident in the end view, as the mean turbulent structures are approximately 20% larger for all three bleed cases than for the blunt base (Fig. 17, top), and the mean structure's major axis is oriented in the streamwise direction rather than circumferentially oriented, as they were in the blunt-base flowfield.

Mathur and Dutton[4] indicate that the peak in turbulent kinetic energy migrates from just prior to the mean reattachment point for bleed case A and the blunt-base case to the approximate location of imaging position *B*1 for bleed cases B and C. As the primary recirculation region is isolated from the outer shear layer and weakened,

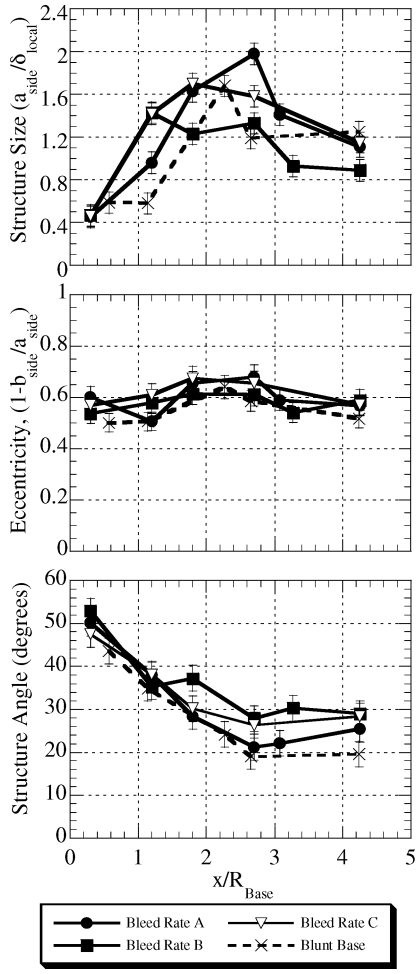

Fig. 16 Side-view correlation statistics at imaging locations *A–E* for the blunt-base and all three base-bleed near-wake flowfields. Vertical bars denote uncertainty of the measurements.

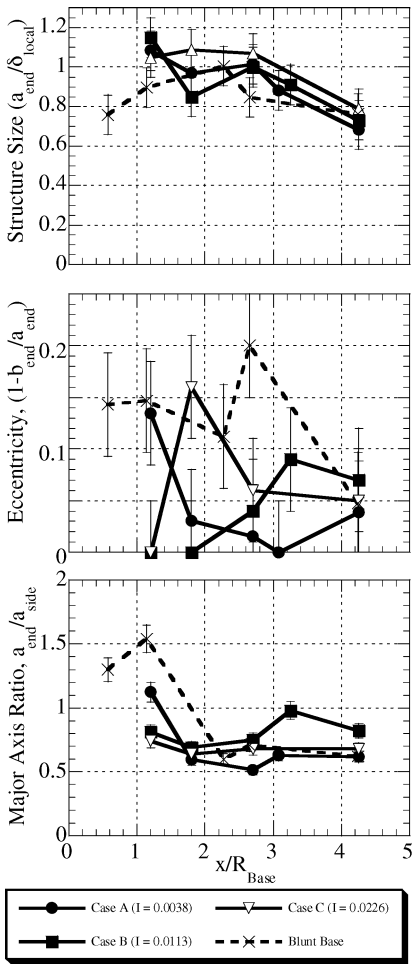

Fig. 17 End-view correlation statistics at imaging locations *A–E* for the blunt-base and all three base-bleed near-wake flowfields. Vertical bars denote uncertainty of the measurements.

the secondary recirculation region becomes responsible for more of the turbulent kinetic energy production in the outer shear layer. This increased production is also evident in that the mean side-view structure size at position $B1$ is approximately 50% higher for bleed cases B and C than for bleed case A (Fig. 16, top).

Despite the turbulent structure growth in this region, the turbulent structures tend to rotate down toward the local streamwise axis (Fig. 16, bottom), just as they did for the blunt-base case. This indicates that the mean side-view structure angle is more sensitive to the shear layer's development toward a self-similar state than it is to local flow conditions. Note, for instance, that for all of the drag-altering cases examined before the mean side-view structure angle is approximately 45 deg just after separation and decreases steadily to approximately 20 deg near the mean reattachment point.[6,14,15] Herrin and Dutton[24] also note that the separation process tends to organize the velocity fluctuations present in the shear layer in the same fashion, regardless of base corner expansion strength or local peak turbulence intensity in the shear layer.

After the initial two imaging positions the three bleed cases do not share the same evolutionary features. Bleed case A reverts to the qualitative trends of the blunt-base case. The mean side-view structure size (Fig. 16, top) reaches its maximum value at position C, in the recompression region, and dramatically decreases at position D, the mean reattachment point. The end-view mean structure size (Fig. 17, top) is also diminished at position D and further relaxes in the developing wake (position E). Because the flow conditions in the developing wake are very similar for bleed case A and the blunt-base case, the side- and end-view structure size at position E (and thus the major axis ratio, Fig. 17, bottom) are virtually identical for the blunt-base and low-bleed cases. The mean side-view structure angle remains slightly higher for bleed case A, likely because of the greater distance of the turbulent structures from the symmetry axis.

At position $B2$ some very interesting trends are present in the correlation statistics for bleed rate B. The mean turbulent structure size, both in the side and end views, decreases to levels below those evident at positions $B1$ and C. The mean side-view structure angle also increases approximately 2 deg from its value at position $B1$. The decrease in structure size and increase in structure angle is mirrored at imaging position D, the mean reattachment point. In a sense, the velocity and turbulence characteristics in the vicinity of the termination of the secondary recirculation region display the same characteristics seen at the mean reattachment point. At $x/R_{base} = 1.8$ (location $B2$) a small annulus exists between the primary and secondary recirculation regions in which bleed fluid can escape the base region without being entrained into either of the recirculation zones. High levels of turbulent kinetic energy exist in this region,[4] and high levels of shear-layer unsteadiness (Fig. 13) and side-view shape factor (Fig. 12) are present. The turbulent structures in this region therefore are presented with an environment that is very similar to that seen in the reattachment region of the blunt-base case (position D).

One might expect that, in the absence of lateral streamline convergence effects, such conditions would lead to a local maximum in side-view turbulent structure size, as seen in the planar base flow.[26] It must be stressed, though, that the evolution of the turbulence in this region of the flow is not driven by the adverse pressure gradient, as it is in the typical reattachment process, but is caused by increased mixing in this region. The shear layer itself increases in thickness, and the turbulent structures grow with the shear layer (Fig. 10). The diminished structure size, when normalized by the local shear-layer thickness, simply indicates that as mass is entrained into the structures it "stand" slightly (i.e., normal to the mean flow direction), and this motion is responsible for the shear layer becoming thicker at a rate faster than the turbulent structures grow in size.

Because bleed case B is very near the optimal bleed condition, the adverse pressure gradient preceding flow reattachment is greatly weakened, and the mean side-view structure size only increases slightly between imaging positions $B2$ and C. The transition from reverse to forward mean velocity along the centerline yields typical results; although, as the mean side-view and end-view structure size drops to below one shear-layer thickness near reattachment, the side-view structure angle increases slightly with respect to the local mean flow direction, and the end-view structure eccentricity increases slightly. Therefore, even though both adverse pressure gradient and streamline convergence effects near reattachment are lessened because of near-optimal bleed conditions, the relative importance of the effects remains relatively unchanged.

For bleed case C the flowfield downstream of position $B1$ is not subject to any effects generated from a primary recirculation region, and so the development of the large-scale turbulent structures present in the outer shear layer displays a different character than either bleed cases A and B or the blunt-base case. The adverse pressure gradient (location C) supports the generation of large, strained structures that rotate down toward the local streamwise axis, and, in the end view, elongate circumferentially (become less eccentric while peaking in size). After the adverse pressure gradient is negotiated, the turbulent structures transition to a shape and size (in relation to the local shear-layer thickness) that is very close to that of the blunt-base case. The abrupt decrease in side-view and end-view structure size usually found at position D is not present in the correlation results of bleed case C.

Conclusions

This work examines the turbulent structures present in the outer shear layer of a supersonic base-bleed flow using the same ethanol planar Mie-scattering technique developed in previous studies. The injection of mass through a central bleed orifice is shown to significantly alter the mean size, shape, and organization of the large-scale turbulent structures in the near wake. These effects are quantified through the use of spatial correlation, shape factor, and steadiness analyses.

At the low-bleed condition (case A, $I = 0.0038$) the bleed jet does not contain sufficient momentum to remain coherent along the axis of symmetry after it exits the bleed orifice, and the bleed fluid interacts almost immediately with the outer shear layer. The ejection of bleed fluid into the outer shear layer leads to a 40% increase in side-view shear-layer unsteadiness and an increase in side-view structure size from the blunt-base case at all imaging positions prior to the last one. Because the bleed flow rate is relatively low and the bleed flow is injected with little momentum, the overall trends evident in the mean structure statistics resemble the blunt-base statistics.

The bleed fluid in case B ($I = 0.0113$) contains sufficient axial momentum to penetrate approximately one base radius into the near wake along the symmetry axis before it is deflected outward as a result of interaction with the primary recirculation region. The ejection of bleed fluid into the outer shear layer generates a local enhancement of side-view shape factor and rms shear-layer position at imaging position $B2$, approximately 1.8 base radii downstream of the base corner, but also causes the mean side- and end-view structure size to decrease with respect to the local shear-layer thickness. This behavior occurs because, in the absence of an adverse pressure gradient, the local shear-layer thickness increases more than the mean structure size.

The recompression shock system is weaker, and the shear layer does not travel as near the symmetry line at the mean reattachment point, as for no bleed, so recompression and streamline convergence effects do not have as strong an effect on the mean turbulent structure statistics in the recompression and reattachment regions of bleed case B. There is only a slight increase in structure size between positions $B2$ and C as a result of the adverse pressure gradient. The characteristic decrease in side-view structure size at the mean reattachment point is present, and so it is concluded that although the effects of adverse pressure gradients and extra strain rates are diminished they still foster the same results at the mean reattachment point.

The image steadiness statistics of the outer shear layer for bleed case C indicate peaks in rms side-view shear-layer position at imaging positions $B1$ and C, centered above the secondary recirculation region and at the location of bleed breakup, respectively. The spatial correlation statistics indicate that, while the outer shear layer borders the secondary recirculation region, the side-view and end-view structure sizes steadily increase, and the turbulent structures rotate down toward the local flow direction. After the termination of the secondary recirculation region, the turbulent structures present in the outer shear layer slowly shrink in size until they quite closely resemble those of the other bleed cases and the blunt-base case.

In the developing wake region (position E) the turbulent structures for all three bleed cases assume sizes and eccentricities very similar to those seen in the blunt-base case. The primary difference in these results is that the mean structure angle is larger for the three bleed cases than for the blunt-base case. A direct relationship seems to exist between end-view core area in the wake (position E) and the mean side-view structure angle.

In addition to the flow visualization and structure quantification study performed here, nonintrusive, instantaneous pressure and temperature measurements, on either a pointwise or planar basis, would add substantial understanding of this complex separated flow.

Acknowledgments

Funding for this research is provided through the U.S. Army Research Office, Grant DAAD19-01-1-0367, with Thomas L. Doligalski as Technical Monitor.

References

[1]Reid, J., and Hastings, R. C., "The Effect of a Central Jet on the Base Pressure of a Cylindrical After-Body in a Supersonic Stream," Royal Aircraft Establishment, Rept. Aero. 2628, Farnborough, England, U.K., Dec. 1959.

[2]Korst, H. H., "A Theory for Base Pressures in Transonic and Supersonic Flow," *Journal of Applied Mechanics*, Vol. 23, No. 4, 1956, pp. 593–600.

[3]Mathur, T., "An Experimental Investigation of the Effects of Base Bleed in Axisymmetric Supersonic Flow," Ph.D. Dissertation, Dept. of Mechanical and Industrial Engineering, Univ. of Illinois, Urbana, IL, July 1996.

[4]Mathur, T., and Dutton, J. C., "Velocity and Turbulence Measurements in a Supersonic Base Flow with Mass Bleed," *AIAA Journal*, Vol. 34, No. 6, 1996, pp. 1153–1159.

[5]Mathur, T., and Dutton, J. C., "Base Bleed Experiments with a Cylindrical Afterbody in Supersonic Flow," *Journal of Spacecraft and Rockets*, Vol. 33, No. 1, 1996, pp. 30–37.

[6]Bourdon, C. J., and Dutton, J. C., "Visualization of a Central Bleed Jet in an Axisymmetric, Compressible Base Flow," *Physics of Fluids*, Vol. 15, No. 2, 2003, pp. 499–510.

[7]Sahu, J., Nietubicz, C., and Steger, J., "Navier–Stokes Computations of Projectile Base Flow with and Without Mass Injection," *AIAA Journal*, Vol. 23, No. 9, 1985, pp. 1247–1255.

[8]Sahu, J., "Supersonic Flow Over Cylindrical Afterbodies with Base Bleed," AIAA Paper 86-0487, Jan. 1986.

[9]Sahu, J., and Heavey, K. R., "Numerical Investigation of Supersonic Base Flow with Base Bleed," *Journal of Spacecraft and Rockets*, Vol. 34, No. 1, 1997, pp. 62–69.

[10]Fu, J.-K., and Liang, S.-M., "Drag Reduction for Turbulent Flow over a Projectile: Part I," *Journal of Spacecraft and Rockets*, Vol. 31, No. 1, 1994, pp. 85–92.

[11]Kaurinkoski, P., and Hellsten, A., "Numerical Simulation of a Supersonic Base-Bleed Projectile with Improved Turbulence Modeling," *Journal of Spacecraft and Rockets*, Vol. 35, No. 5, 1998, pp. 606–611.

[12]Bourdon, C. J., and Dutton, J. C., "Planar Visualizations of Large-Scale Turbulent Structures in Axisymmetric Supersonic Separated Flows," *Physics of Fluids*, Vol. 11, No. 1, 1999, pp. 201–213.

[13]Bourdon, C. J., and Dutton, J. C., "Shear Layer Flapping and Interface Convolution in a Separated Supersonic Flow," *AIAA Journal*, Vol. 38, No. 10, 2000, pp. 1907–1915.

[14]Bourdon, C. J., and Dutton, J. C., "Effects of Boattailing on the Turbulence Structure of a Compressible Base Flow," *Journal of Spacecraft and Rockets*, Vol. 38, No. 4, 2001, pp. 534–541.

[15]Bourdon, C. J., and Dutton, J. C., "Mixing Enhancement in Compressible Base Flows via Generation of Streamwise Vorticity," *AIAA Journal*, Vol. 39, No. 8, 2001, pp. 1633–1635.

[16]Herrin, J. L., "An Experimental Investigation of Supersonic Axisymmetric Base Flows Including the Effects of Afterbody Boattailing," Ph.D. Dissertation, Dept. of Mechanical and Industrial Engineering, Univ. of Illinois, Urbana, IL, July 1993.

[17]Herrin, J. L., and Dutton, J. C., "Supersonic Near-Wake Afterbody Boattailing Effects on Axisymmetric Bodies," *Journal of Spacecraft and Rockets*, Vol. 31, No. 6, 1994, pp. 1021–1028.

[18]Sauter, J. M., "Design of an Axisymmetric Supersonic Wind Tunnel and Experimental Study of Supersonic Power-Off Base Flow Phenomena," M.S. Thesis, Dept. of Mechanical and Industrial Engineering, Univ. of Illinois, Urbana, IL, July 1989.

[19]Smith, K. M., "The Role of Large Structures in Compressible Reattaching Shear Flows," Ph.D. Dissertation, Dept. of Mechanical and Industrial Engineering, Univ. of Illinois, Urbana, IL, Aug. 1996.

[20]Samimy, M., and Lele, S., "Motion of Particles with Inertia in a Compressible Free Shear Layer," *Physics of Fluids A*, Vol. 3, No. 8, 1991, pp. 1915–1923.

[21]Wegener, P. P., Clumpner, J. A., and Wu, B. J. C., "Homogeneous Nucleation and Growth of Ethanol Drops in Supersonic Flow," *Physics of Fluids*, Vol. 15, No. 11, 1972, pp. 1869–1876.

[22]Clemens, N. T., "An Experimental Investigation of Scalar Mixing in Supersonic Turbulent Shear Layers," High Temperature Gasdynamics Lab., Dept. of Mechanical Engineering, HTGL Rept. T-274, Stanford Univ., Stanford, CA, June 1991.

[23]Smith, K. M., and Dutton, J. C., "Evolution and Convection of Large-Scale Structures in Supersonic Reattaching Shear Flows," *Physics of Fluids*, Vol. 11, No. 6, 1999, pp. 2127–2138.

[24]Herrin, J. L., and Dutton, J. C., "Effect of a Rapid Expansion on the Development of Compressible Free Shear Layers," *Physics of Fluids*, Vol. 7, No. 1, 1995, pp. 159–171.

[25]Messersmith, N. L., and Dutton, J. C., "Characteristic Features of Large Structures in Compressible Mixing Layers," *AIAA Journal*, Vol. 34, No. 9, 1996, pp. 1814–1821.

[26]Smith, K. M., and Dutton, J. C., "Investigation of Large-Scale Structures in Supersonic Planar Base Flows," *AIAA Journal*, Vol. 34, No. 6, 1996, pp. 1146–1152.

M. S. Miller
Associate Editor